Available online at www.sciencedirect.com
ScienceDirect
Trans. Nonferrous Met. Soc. China 31(2021) 952−966
Transactions of Nonferrous Metals Society of China
www.tnmsc.cn

Improvement of in vitro corrosion, wear, and mechanical properties of newly developed Ti alloy by thermal treatment for dental applications

Mohamed HUSSEIN[1], Akeem Y. ADESINA[1], Madhan KUMAR[1],
Mohamed AZEEM[2], Ahmad SOROUR[1,2], Nasser AL-AQEELI[3]

1. Center of Research Excellence in Corrosion, King Fahd University of Petroleum & Minerals, Dhahran 31261, Saudi Arabia;
2. Department of Mechanical Engineering, King Fahd University of Petroleum & Minerals, Dhahran 31261, Saudi Arabia;
3. Mechanical Engineering Department, College of Engineering, King Saud University, Riyadh 11421, Saudi Arabia

Received 11 January 2020; accepted 5 January 2021

Abstract: The effects of thermal treatments on the structure, mechanical properties, wear resistance, and in vitro corrosion protection in artificial saliva (AS) were investigated for a newly developed Ti20Nb13Zr (TNZ) alloy. XRD and SEM analyses were used for structural and microstructural analysis. The in vitro corrosion properties of the samples were investigated using electrochemical impedance spectroscopy and linear polarization resistance techniques up to an immersion time of 168 h. The tribological characteristics were evaluated with a linear reciprocating tribometer. SEM analysis showed that solution treatment and aging influenced the size and distribution of α phase. The air-cooled and aged samples exhibited the highest microhardness and macrohardness, for which the wear resistances were 25% and 30% higher than that of the untreated sample, respectively. The cooling rate significantly influenced the corrosion resistance of the TNZ samples. The treated samples showed a reduced corrosion rate (50%) for long immersion time up to 168 h in AS. The furnace-cooled and aged samples exhibited the highest corrosion resistance after 168 h of immersion in AS. Among the treated samples, the aged sample showed enhanced mechanical properties, wear behavior, and in vitro corrosion resistance in AS.

Key words: heat treatment; Ti-based alloy; microstructure; mechanical properties; wear; corrosion; biomaterials

1 Introduction

Ti and Ti alloy TiAl6V4 (Ti64) are used in dentistry and orthopedics due to higher bio-compatibility, enhanced mechanical properties and corrosion protection [1−5]. Corrosion studies of Ti64 alloy have been conducted in artificial saliva (AS) and oral rinse for dental applications [6,7]. For dental applications, the sintered Ti64 alloy exhibited better performance than the casted alloy under corrosion and tribocorrosion conditions in saliva [4]. The electrochemical behavior and galvanic effects of various titanium implants in artificial saliva showed that the best performance was obtained when using Ti/Ti6Al4V and Ti/CoCr; furthermore, comparisons revealed that these material combinations provided superior performance to Co-based alloys [8]. However, the release of metal ions from the surface leads to inflammation [9].

Moreover, reports have shown that V and Al exhibit toxicity effects [10]. Due to the limited wear resistance of Ti alloys, implants made from these materials are prone to the release of metallic ions, which may enter the bloodstream and cause

Corresponding author: Mohamed HUSSEIN; E-mail: mahussein@kfupm.edu.sa
DOI: 10.1016/S1003-6326(21)65552-8

inflammation and pain [11]. Moreover, this surface degradation may lead to the subsequent failure of the implant [12]. Therefore, numerous other Ti alloys have been developed and introduced as implant materials, including Ti6Al7Nb alloy [13] and Ti20Nb13Zr (TNZ) alloy [2,14,15], which are categorized as α+β and near β alloys, respectively. To increase the service lives of implants, the mechanical properties, corrosion behavior, and wear resistance of Ti biomedical alloys require further enhancement [16]. Heat treatment (HT) was reported to influence the performance of Ti and Mg alloys [17,18]. Aging TiMoZrFe alloy results in increased strength and modulus due to precipitation of α and ω phases in the β matrix [19]. The mechanical properties of TNZS-xO alloys are influenced by aging treatment [20]. The high cooling rate of treated TiNbTaZr samples leads to the formation of β, α'' and ω phases. The corrosion resistance of Ti alloys is affected by solution treatment [21]. The surface hardness of Ti−30Nb−1Fe alloys is improved by aging treatment [22]. HT provides the best combination of the mechanical characteristics [23,24]. Although several investigations have been reported on the HT of Ti−6Al−4V, few studies have been reported on the HT of Ti−Nb−Zr alloys. HT of TNTZ alloys exhibits a good combination of ductility and strength [25]. The aging affects the mechanical characteristics of the Ti alloy due to precipitation of α phase [26]. Compared to commercial Ti64 alloy, TNZ alloy exhibits better mechanical properties [2], in vitro corrosion resistance in simulated body fluid (SBF), and bioactivity [15]. Recently, HUSSEIN et al [27] have studied the effect of HT on the biocorrosion properties of TNZ in SBF for implant applications. To determine the potential of utilizing thermally treated TNZ alloy for dental applications, this research aims to examine the effect of HT of TNZ alloy on the corresponding microstructure, hardness, wear rate, and in vitro corrosion in AS. The samples were heated above the β-transus temperature and then cooled in water, in air, and in a furnace. Then, the water-cooled samples were aged.

2 Experimental

The samples used in the current study were 20 mm discs with 4 mm in thickness composed of a newly fabricated Ti20Nb13Zr (at.%) (TNZ) alloy. This new alloy was developed from the nontoxic and biocompatible elements of Ti, Nb, and Zr (purity of 99.9%) via a powder metallurgy process (the blended powder was milled for 10 h in argon and then sintered with spark plasma sintering) at 1200 °C. The details of TNZ fabrication were reported in Refs. [2,15]. The molybdenum equivalent was calculated to be 14.364 for Ti−20Nb−13Zr alloy, as reported previously [15], which is above the value of 10.0 that is essential to stabilize β-Ti [14]. The HT was performed in a tube furnace (GSL−1700X, MTI) under a high-purity Ar environment. The samples were placed in an alumina crucible, which was loaded in the furnace and heated to 900 °C at 10 °C/min. The samples were held isothermally at 900 °C for 1 h before being water-cooled (WC), air-cooled (AC), or furnace-cooled (FC). The quenched sample was aged at 500 °C for 5 h and then cooled in air.

After HT, the samples were ground with a sequence of 200, 300, 400, 600, and 800-grit SiC papers, after which the samples were polished to obtain a mirror-like surface. Then, the samples were etched in a solution (20% HF in water). The phases of the treated alloy were characterized via XRD (Rigaku, Kurary, Japan) at 40 kV and 30 mA with a scan range of 20° to 90°. The microstructure of the alloy was investigated via SEM (JEOL, Japan) at 15 kV. The mechanical properties of the alloy were assessed by performing microhardness and macrohardness measurements with a Vickers hardness tester (Buehler MMT−3, USA) at three different loads of 3, 5, and 20 N. The hardness value represents the average of 10 readings taken at least 1 mm apart at all sites on the samples.

The corrosion resistance of the thermally treated TNZ samples was evaluated with a Gamry Reference 3000 electrochemical workstation. The tested electrolyte−AS solution was prepared, and the in vitro corrosion test was conducted using the previous reports to evaluate the performance of the treated TNZ alloy as dental implants [28,29]. A conventional three-electrode assembly was used to perform the electrochemical impedance spectroscopy (EIS) and linear polarization resistance (LPR) tests up to 168 h. Treated TNZ samples with an exposure area of 1.76 cm^2 were used as the working electrode, whereas a graphite

rod and a saturated Ag/AgCl electrode were used as the auxiliary and reference electrodes, respectively. Before each electrochemical experiment, the treated TNZ sample was immersed in AS for approximately 1 h to reach a stable open circuit potential (OCP). The EIS examinations were performed using the frequency range of 100 kHz to 0.01 Hz with an amplitude of 10 mV. The EIS results were further analyzed with Echem Analyst software, and the obtained results were displayed in Nyquist and Bode plots. An LPR test was also carried out by applying a potential of ±25 mV from the OCP for up to 168 h.

The tribological characteristics of the untreated (UT) and thermally treated samples were evaluated with a linear reciprocating tribometer (TR−282, Ducom Instruments, India) and subsequently compared. A hardened steel ball with a radius of 3 mm was used as the counterpart under the environmental test conditions (an ambient temperature of (23±5) °C and relative humidity of (50±5)%). A normal load of 10 N was applied for a distance of 100 m, which was accomplished by reciprocating at a frequency of 5 Hz; this frequency corresponds to a linear reciprocating velocity of 0.05 m/s over a stroke length of 5 mm. A weight-loss method with the aid of an analytical weight balance (AB−224, Phoenix Instruments, USA) was used to quantify the specific wear rate, which is expressed as the mass loss (mg) per normal load (kN) per total reciprocating distance (m). An optical profilometer (Contour GT-K, Bruker, USA) was used to observe the 3D profile of the wear track and to corroborate the results obtained from the mass-loss measurements.

3 Results and discussion

3.1 Microstructure and structure

XRD pattern of as-sintered (untreated) (α+β) TNZ alloy is presented in Fig. 1(a). The XRD pattern confirms the presence of both phases (β and α). The higher intensity of β phase compared to α phase indicates the higher amount of β phase compared to α phase. The microstructure of the untreated sample consists of β (bcc) matrix (whiter area) surrounded by α (hcp) phase (darker area), as shown in Fig. 1(b).

The newly developed (α+β) TNZ alloy was subjected to HT under different conditions. SEM

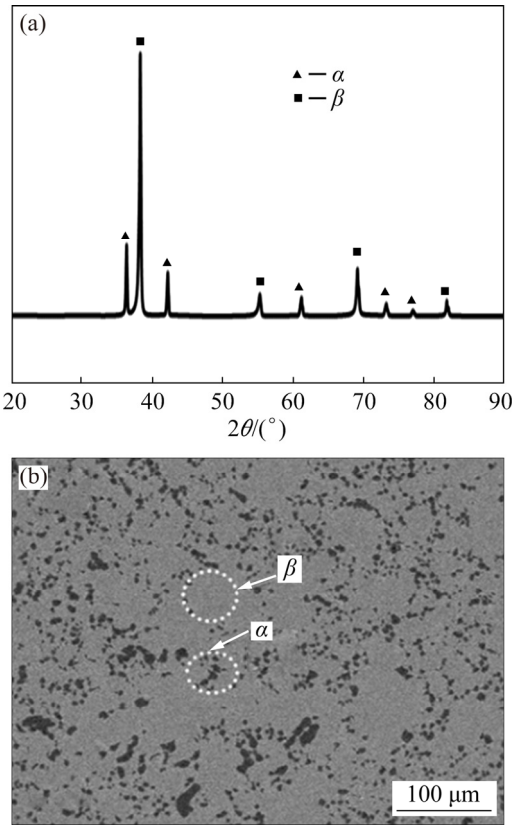

Fig. 1 XRD pattern (a) and SEM image (b) of untreated TNZ alloy

was used to analyze the microstructural evolution after various treatments. After solution treatment, the WC sample primarily contained the β matrix with a very small amount of α phase at the grain boundary, as shown in Fig. 2(a). A high-magnification image showed the presence of α phase, which was needle-like, in the β matrix. The major portion of α phase in the WC samples was transformed into β phase due to the fast cooling rate. However, the amounts of α phase in the AC and FC samples increased due to the decrease in cooling rate, as shown in Figs. 2(b) and (c), respectively. Moreover, due to reduced cooling rate compared to the WC sample, less α phase transformed to β phase, and the volume fraction of α increased, as greater time was given for α phase to grow. The WC sample was then subjected to aging at 500 °C for 5 h. The microstructure of the aged samples revealed that both grain boundary α and intergranular α phases were formed (Fig. 2(d)). Additionally, a fine secondary α precipitate, which was needle-like, was formed after aging.

These phases were also confirmed from the XRD patterns, as presented in Fig. 3. The XRD

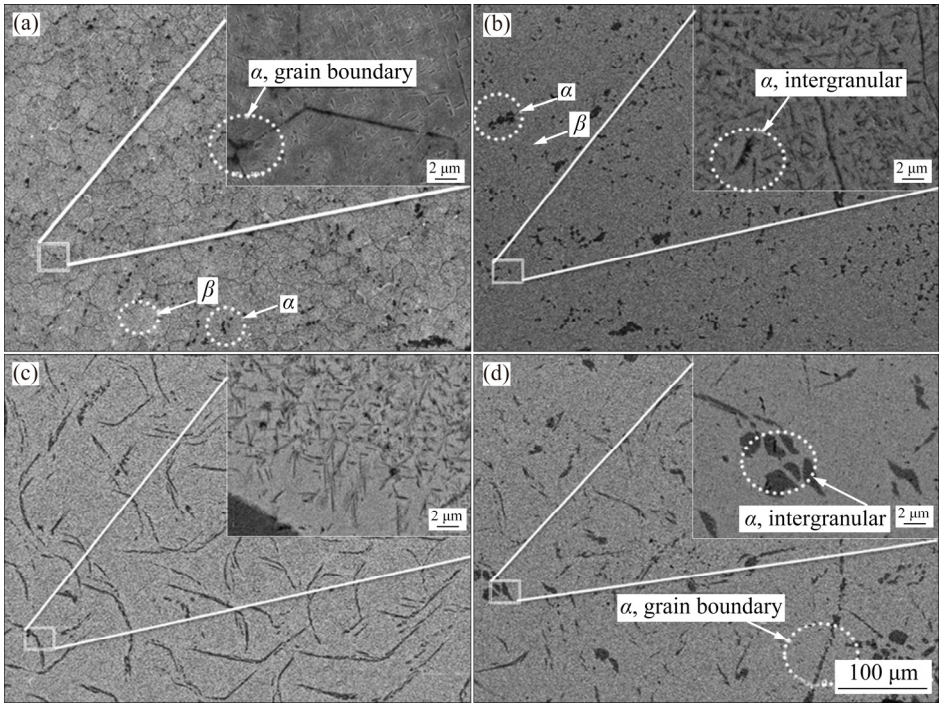

Fig. 2 SEM micrographs of thermally treated TNZ samples under different conditions: (a) WC; (b) AC; (c) FC; (d) Aged

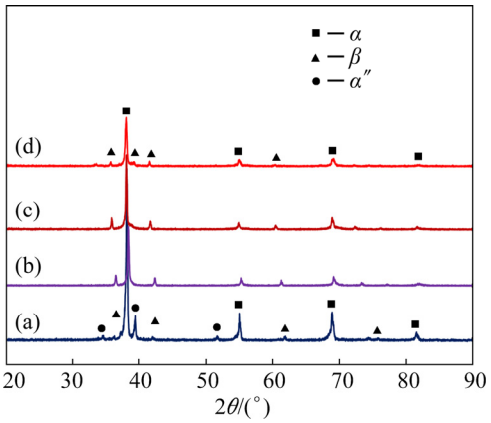

Fig. 3 XRD patterns of thermally treated TNZ samples under different conditions: (a) WC; (b) AC; (c) FC; (d) Aged

pattern for the WC sample mainly showed the β phase with a high-intensity peak and low-intensity peaks of α phase, which indicates small amount of α phase in this sample. Moreover, there are small peaks observed in the WC sample, which are indexed to be α'' martensitic phase. This martensitic phase may be considered as an intermediate phase between β and α [30]. For the AC, FC, and aged samples, the intensity of the α peaks was higher than that in the WC samples, indicating that the former samples have a higher volume fraction of α phase; these findings were confirmed from the SEM images shown in Fig. 2. The martensitic α'' phase formed after water cooling became unstable and was converted to either β or α+β after aging, as noted in an earlier report [31]. A proper microstructure is essential for an alloy to be used in biomedical applications, as the microstructure influences the mechanical, physical, and corrosion properties of the alloy. In this study, the alloy microstructure was influenced by different HT processes. TiNbZr alloy consists of α+β phase, and the amount of β phase in the alloy was influenced by the solution temperature, and consequently, the response to aging [32]. Based on the alloying elements, two phases are stabilized: α phase and β phase. Also, based on their structures, the Ti alloys can be classified as α, near-α, α+β, or β alloys [33]. The β phase possesses high workability, excellent fatigue behavior, and good hardening ability. The HT response of Ti alloys originates from the instability of the β phase at lower temperatures. The solution treatment of Ti alloy produces a high amount of β phase. The supersaturated phase decomposes, and the aging controls the microstructure and strength. The aging increases the elastic modulus and hardness of β phase due to the precipitation of fine α phase. It has been reported that α phase is formed after cooling β phase below

the β-transus temperature [34]. Additionally, the shape of α phase is influenced by the thermal treatment conditions [35]. Furthermore, the previous reports showed that the martensitic phase is formed during solution treatment above the β-transus temperature of titanium alloy [36,37], which agrees with the obtained results.

3.2 Vickers microhardness and macrohardness

The Vickers hardness (HV) of the treated samples is depicted in Fig. 4 at three different loads. Among the samples subjected to solution treatment at 900 °C, the AC sample exhibited the highest Vickers hardness value. Due to higher cooling rate during water cooling, the WC sample contains less α phase in the microstructure. Besides, the Vickers hardness value of the WC sample is limited by the presence of the soft martensitic phase. In contrast, the AC sample had a higher amount of α phase, which contributed to its increased hardness. The fine intergranular α phase precipitated after aging, thereby increasing the volume fraction of grain boundary α and enhancing the Vickers hardness value: the hardness value of the aged sample was HV (587.2±6.3), whereas that of the WC sample was HV (564±8.9). These results confirm the XRD and SEM observations. The aging increases the hardness of Ti alloys due to the precipitation of the fine α phase in a matrix of the β phase. The solution treatment of Ti alloy produces a high amount of β phase due to the transformation of α to β. The quenching after the solution treatment maintains the β phase. However, the subsequent aging after solution treatment leads to the decomposition of the β phase and the martensitic phase, resulting in high strength. A similar trend of results has been obtained from the thermomechanical treatment of TNZV alloy [38]. According to Ref. [39], the microstructure and compositions mainly control the mechanical characteristics of a material. In addition, more specifically for α+β titanium alloys, the mechanical characteristics are affected by the relative amount of each phase and their corresponding morphologies, and these parameters could be altered by the HT [40]. The dispersion of α phase in the β matrix contributes to increasing the hardness of heat-treated samples. Moreover, this phenomenon enhances the dislocation motion at the α/β interface, thereby increasing the strength of the matrix.

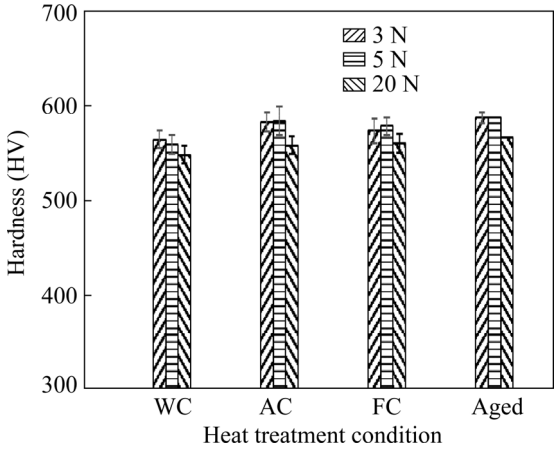

Fig. 4 Hardness of thermally treated TNZ samples

The phases of the UT alloy are the β phase (BCC) crystal structure and α phase (HCP).

The WC sample includes a small amount of α and the martensitic α'' phase (orthorhombic) structure. Due to relatively high cooling rate for the WC sample, solute atoms have less time to precipitate from β phase, which results in less amount of α phase compared to AC and FC samples.

For AC and FC samples, the cooling rate was reduced, so the atoms had more time and energy, and could obtain sufficient energy to break the bond of the adjacent atom and diffuse. Then, the diffused atoms could rearrange, and hence more α phase was formed. α phase (HCP) crystal structure has a lower slip system compared to β phase (BCC). Therefore, a high load is required for plastic deformation for α phase, which will result in increased strength. Moreover, fine α grain, which transforms from the β matrix during the AC, FC, and precipitate during aging, will increase the interaction between the dislocations, which inhibit the movement of dislocation and contribute to improving the hardness [41]. The observed difference between microhardness and macro-hardness was due to the indentation size effect [42], which resulted from numerous aspects: surface effects [43], friction [44], or strain hardening gradient [45].

3.3 In vitro corrosion in AS

Figure 5(a) displays the LPR plots of the thermally treated and bare samples in AS. The results show that the relation of current density vs potential illustrates good linearity near corrosion

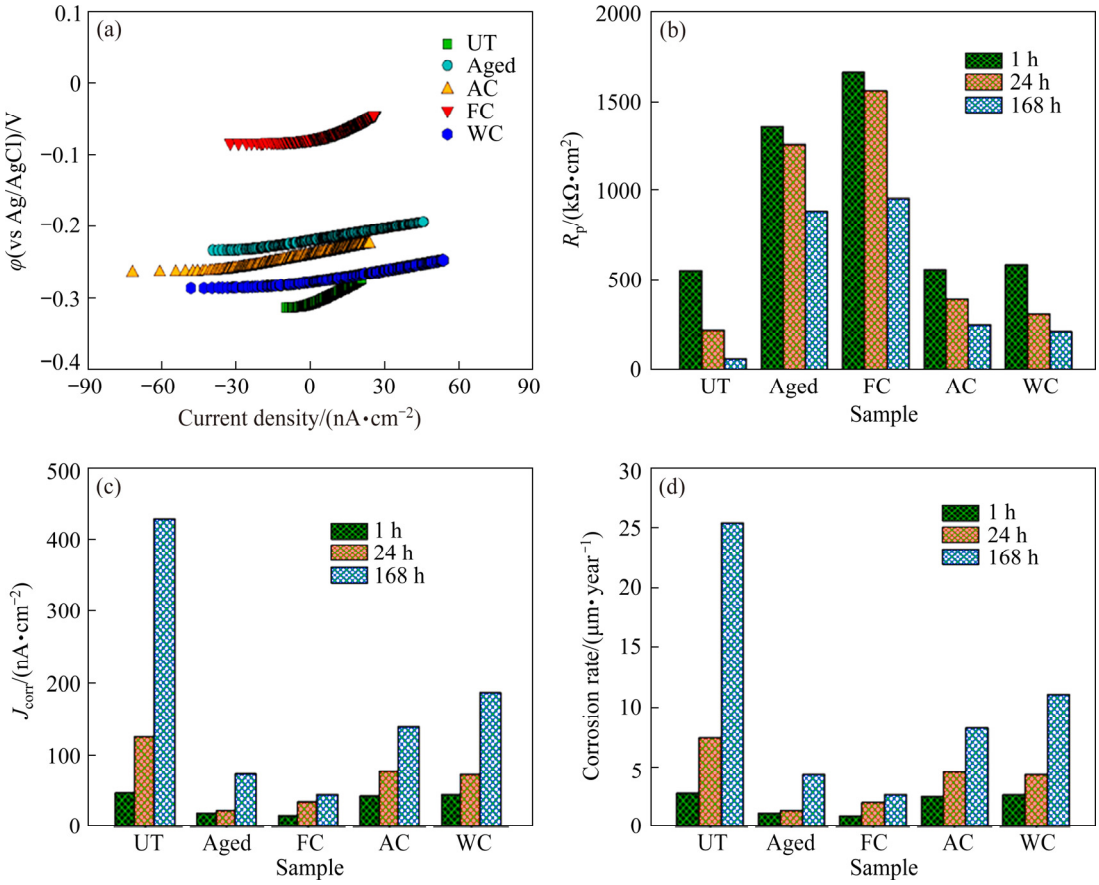

Fig. 5 Plots of φ (a), R_p (b), J_{corr} (c), and corrosion rate (d) of UT and treated samples

potential φ_{corr}. From the obtained LPR plots, the electrochemical parameters, including the polarization resistance (R_p) corrosion current density (J_{corr}), and corrosion rate, were calculated, and the obtained values were plotted in Figs. 5(b−d), respectively. The decrease in the R_p values with respect to the increase of the immersion time was observed in the case of the untreated TNZ sample, and this variation was lower in the case of the treated TNZ samples (Fig. 5(b)). For the untreated TNZ sample, as the immersion time increased from 1 to 24 h, R_p slightly decreased from 558.55 to 224.45 kΩ·cm^2; a dramatic reduction in R_p was observed when the immersion extended up to 168 h, wherein R_p was only 60.25 kΩ·cm^2. As the value of J_{corr} is in direct proportion to the corrosion rate, a lower value of J_{corr} normally indicates a higher corrosion resistance [46]. From Fig. 5(c), all the treated TNZ samples exhibited lower J_{corr} values than the untreated sample; particularly, the aged and FC samples exhibited the lowest J_{corr} values. Based on the obtained corrosion current density (J_{corr}) values, the corrosion resistance of the samples from high to low is characterized as follows: FC > aged > AC > WC > untreated TNZ sample. Figure 5(d) clearly showed that the untreated TNZ sample exhibited the highest corrosion rate, for which the value was nearly twofold that of the treated TNZ samples. Besides, the treated TNZ samples exhibited a more stable and uniform corrosion rate as the exposure period increased. Furthermore, both the aged and FC samples showed a lower corrosion rate than the other samples, which indicated that these samples had better corrosion resistance than other samples in AS. Particularly for the FC sample, the corrosion rate was still very low after 168 h of exposure in AS. The improved corrosion resistance of the FC sample was obtained because of the slow cooling rate and the high volume fraction of α phase, which further facilitated the formation of a more compact and protective surface film [27].

Figure 6(a) presents the Nyquist plots of the heat-treated and untreated alloy after 1 h of immersion in AS. The Nyquist plot was characterized by a large quarter-capacitive arc, which represents single relaxation time constant behavior in the investigated frequency range. A closer comparison of the Nyquist plots of the

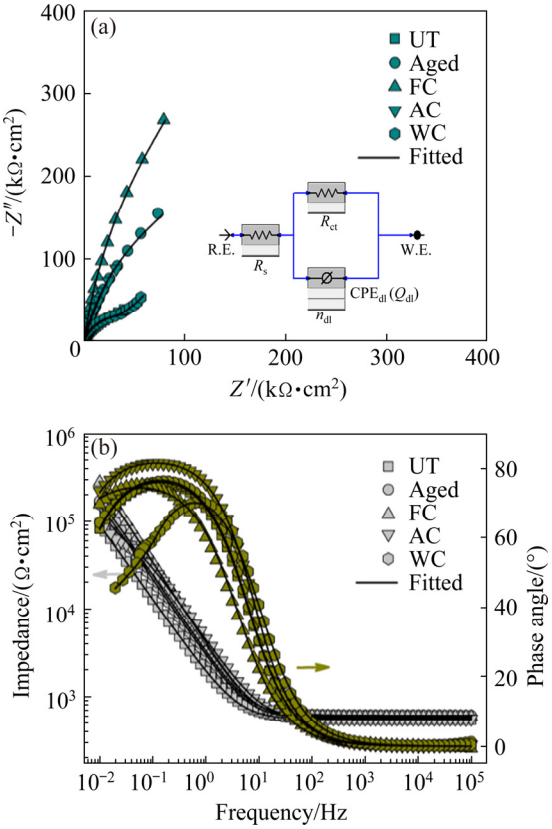

Fig. 6 Nyquist (a) and Bode (b) plots of UT and treated samples after 1 h of immersion in AS

treated and untreated samples shows that the diameter of the curve/charge transfer resistance (R_{ct}) increases in all the treated TNZ samples after 1 h of immersion in AS. The higher R_{ct} values in the treated samples demonstrate the impact of the microstructure on the corrosion performance of the treated TNZ samples [27]. Figure 6(b) presents the Bode plots of the heat-treated and untreated alloy after 1 h of immersion in AS. At high frequencies ranging from 10^5 to 10^3 Hz, the impedance modulus ($|Z|$) became constant, indicating that the impedance was controlled by electrolytic resistance. In a wide frequency range (lower and middle frequencies), the impedance response exhibited a linear behavior with a slope of approximately −1 in all investigated samples, which was the distinctive response of the capacitive performance of a passive layer [47]. At the lowest frequency of 0.01 Hz, the value of $|Z|$ for the untreated TNZ sample was found to be $10^5\ \Omega\cdot cm^2$ after 1 h of immersion in AS. After heat treatment, the $|Z|$ values for the aged, FC, AC, and WC samples were 185.50, 280, 156.45, and 122 $k\Omega\cdot cm^2$, respectively. In the Bode phase angle plots (Fig. 6(b)), three distinctive regions were observed in the investigated frequency range. The phase angle decreased to 0° in the higher frequency regions due to the response of the solution resistance. In contrast, in the middle frequency region, the maximum phase angle reached above 80° in all investigated samples, demonstrating the near capacitive response of the passive film; particularly, the FC samples exhibited the highest phase angle of 82°. In the lowest frequency range, lower phase angles were observed in all cases. The EIS measurements up to an immersion time of 168 h evaluated the influence of the exposure period on the corrosion resistance of the samples in AS, which is a primary prerequisite for biomedical, dental implants. The EIS results are presented in Figs. 7 and 8.

Furthermore, to validate the obtained EIS results, the experimental EIS curves were simulated using a proper equivalent circuit model (the inset in Fig. 6(a)). Based on the obtained large semicircular capacitive arc and the one time constant in the spectra, the modified Randle's circuit [$R_s(R_{ct}Q_{dl})$] (where R_s is the solution resistance; R_{ct} is the resistance of charge transfer; Q_{dl} is the constant phase element (CPE) of double layer capacitance) was used to fit the obtained EIS data [15]. This EIS circuit model contains a parallel combination in series, in which the solution resistance exists between the working and reference electrodes. A constant phase element (CPE, Q) could be employed on behalf of the capacitor, balancing the nonideal behavior due to the influence of variations from the surface heterogeneities of the samples. The parameter R_{ct}, which is directly associated with the rate of metal dissolution, is the resistance of charge transfer through the passive film; generally, a higher R_{ct} value signifies enhanced corrosion resistance. From Table 1, the R_{ct} values of the FC and aged samples were substantially higher than those of the other samples, indicating that the corrosion reaction was efficiently inhibited by the metal/electrolyte interface. Furthermore, the lowest Q_{dl} values of the aged and FC samples revealed less dissolution and enhanced passivity. Moreover, the highest n_{dl} (n_{dl} is the exponent of the CPE of double layer) values of these samples after 168 h of exposure further corroborated the maximum uniformity of the passive film developed on the sample surface, which indicated improved corrosion resistance in AS.

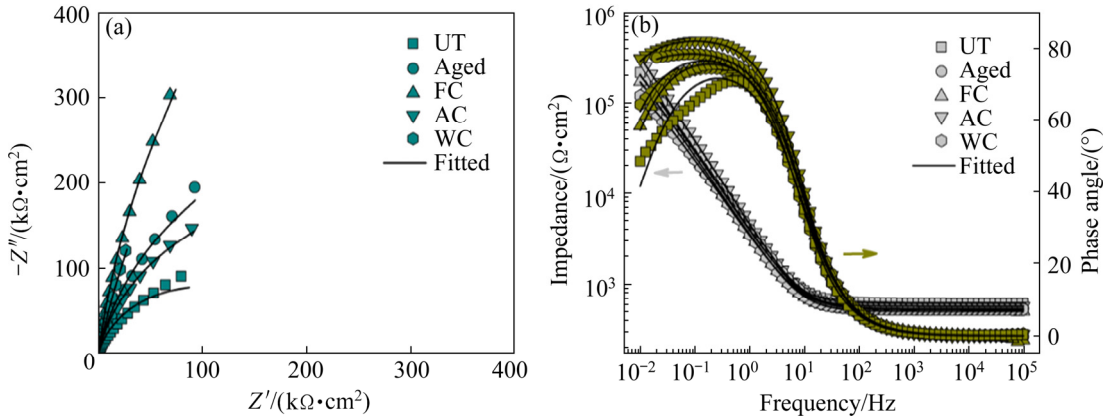

Fig. 7 Nyquist (a) and Bode (b) plots of UT and treated samples after 24 h of immersion in AS

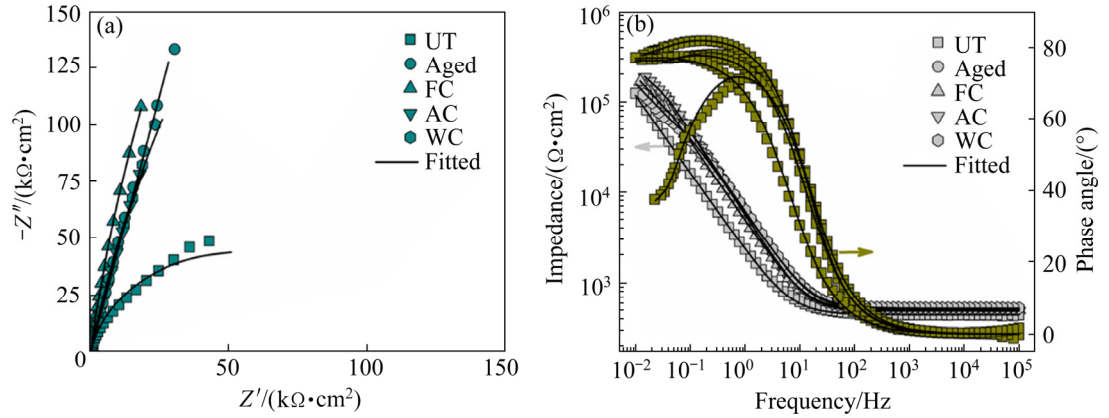

Fig. 8 Nyquist (a) and Bode (b) plots of UT and treated samples after 168 h of immersion in AS

Table 1 EIS parameters for UT and treated samples in AS

Parameter	UT			Aged			FC			AC			WC		
	1 h	24 h	168 h	1 h	24 h	168 h	1 h	24 h	168 h	1 h	24 h	168 h	1 h	24 h	168 h
R_s/($\Omega\cdot cm^2$)	125	123	136	116	123	143	135	141	129	128	124	137	125	138	144
R_{ct}/($k\Omega\cdot cm^2$)	110	101	84	185	182	175	280	271	252	156	143	123	122	117	107
Q_{dl}/($\mu F\cdot cm^2$)	56	89	123	21	42	58	15	26	34	32	47	67	41	57	69
n_{dl}	0.96	0.94	0.89	0.96	0.96	0.95	0.97	0.96	0.95	0.96	0.92	0.91	0.95	0.93	0.90

In general, the mode of microstructure regulates the size and extent of solute segregation in Ti alloys. After solution treatment, the WC sample exhibited a majority of β matrix with a minor amount of α phase at the grain boundary, whereas the amount of α phase increased for AC and FC samples due to the slow cooling rate. Also, less amount of α phase changed to β phase due to this slow cooling rate in comparison with the WC sample, and the volume fraction of α phase increased by reducing the cooling rate since a sufficient period was given for α phase to grow [31]. The WC sample was then subjected to aging at 500 °C for 5 h, and the microstructure of aged samples exhibited both a grain boundary and intergranular α phases. The microstructure of the FC sample showed a matrix of pre-existing β grain with laths on it [48]. The volume fraction of the α phase in the FC sample was higher in comparison with those of the AC and WC samples, as the volume fraction was strongly influenced by the cooling rate. FC encouraged the transformation of β phase to α phase and a higher number of nucleation sites for α phase [49]. The microstructure of the FC

consisting of a higher volume fraction of α phase is considered to be the desired structure for enhanced corrosion resistance due to more homogeneity in the phases. Improved corrosion protective performance of the FC sample is possible because of slow cooling rate with higher volume fraction of α phase in comparison with AC and WC on the surface of treated TNZ samples, which further facilitated to form more compact and protective nature of the surface film.

3.4 Tribological properties

The coefficient of friction (CoF) as a function of the reciprocating distance is shown in Fig. 9 for all treated samples. The samples exhibited similar CoF characteristics during the sliding process, and the HT barely influenced the behavior. Furthermore, the CoF curves of the UT (untreated sample), FC, AC, and WC samples were steadier than that of the aged sample, which experienced a fluctuating, unsteady CoF curve, especially after a long sliding distance. This finding can be attributed to the increased hardness of the aged sample, provided by the precipitation of the fine α phase in the β matrix during aging. However, this fluctuation does not cause a significant change in the average steady state CoF, as shown in the inset of Fig. 10. The samples exhibited similar CoF values of 0.54±0.01, which is considered typical for commercial Ti alloys under similar wear test parameters and conditions; this conclusion has also been reported by previous investigators [50].

The similarity in the CoF values despite different heat treatments can be associated with the

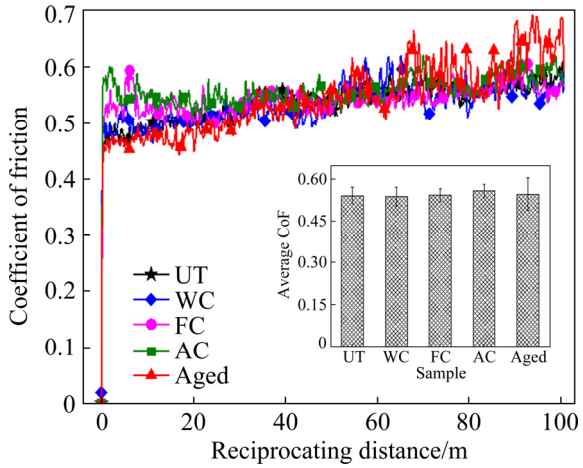

Fig. 9 Coefficient of friction as function of reciprocating distance for UT and treated samples

intrinsic properties of rapid oxide formation in TiNbZr alloys when exposed to atmospheric conditions. The sliding effect also increases the interfacial temperature, thereby increasing the propensity for the formation of a thin oxide film. Accordingly, the interfacial conditions and characteristics remain similar throughout the sliding duration, as new oxide films are readily formed after wearing action.

The 3D profilometer images of the wear track showing the wear depth are shown in Fig. 10, whereas the corresponding wear rate of the samples is displayed in Fig. 11. The wear depth and by extension the wear volume slightly increased in the following order: UT > FC > WC > AC > aged. The UT sample possessed the highest wear rate of 5.4 ng/(kN·m), whereas a slight improvement of approximately 5% and 7.5% was attained for the FC and WC samples, respectively. However, for the AC and aged samples, the wear resistance was enhanced by approximately 25% and 30%, respectively. The large particle size of α phase in the FC samples and the high percentage of the β phase in the WC samples, as shown in the XRD analysis, had a slight effect on reducing the wear rate of the treated alloys due to the low hardness of these samples. On the other hand, the increased percentage and smaller size of the phase in the AC sample improved the mechanical properties, provided this sample had high wear resistance. Similarly, for the wear resistance of the aged sample, the precipitation of very fine α phase and the decrease in the soft β phases provided enhanced mechanical and wear resistance properties, as displayed in Fig. 11.

Figure 12 depicts the SEM micrographs of the wear tracks and the corresponding high magnification images to elaborate the wear mechanisms. From the inserts in Figs. 12(a−e), it can be seen that a significant amount of debris is generated, which can be associated with the brittle nature of the TNZ samples. This debris decreases with the heat treatment, and the lowest debris generated can be attributed to the aged sample. Additionally, the debris is associated with the size of the wear track, which can be observed in the SEM images in Figs. 12(a–e), which also collaborate the 3D optical profilometer images in Fig. 10. The debris affects the wear of the samples by acting as a third body in a three-body abrasive

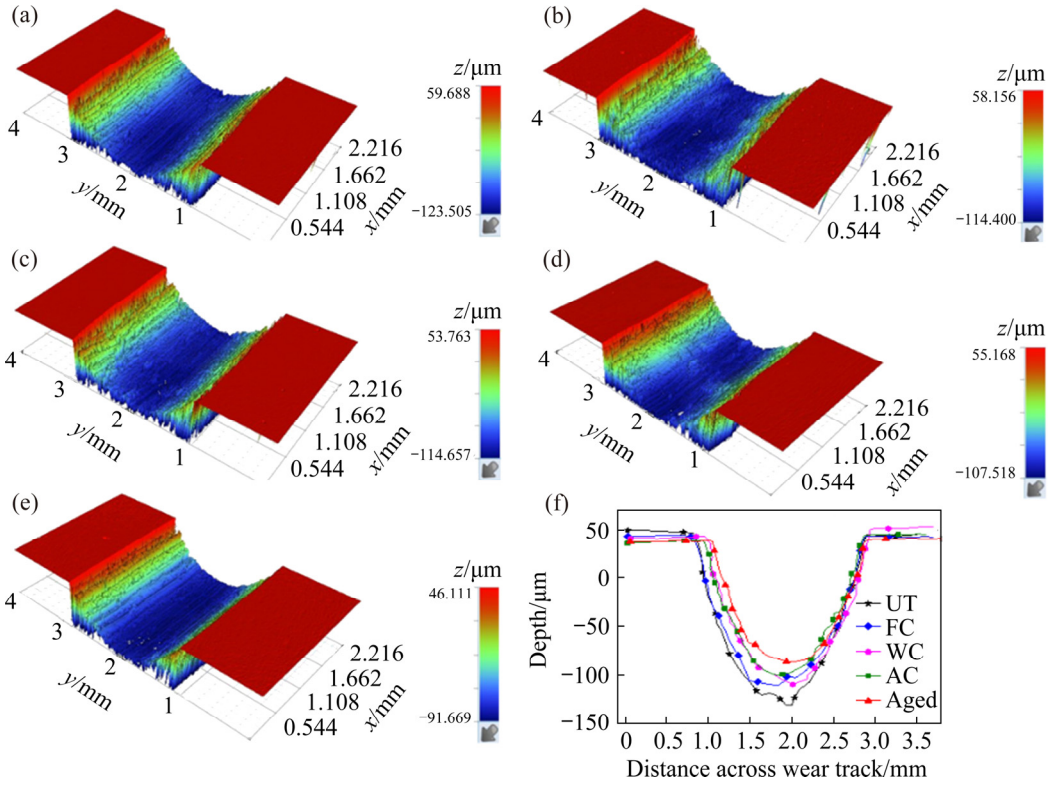

Fig. 10 3D optical profilometer images of wear track of samples: (a) UT; (b) FC; (c) WC; (d) AC; (e) Aged; (f) 2D wear track profile of UT and treated samples

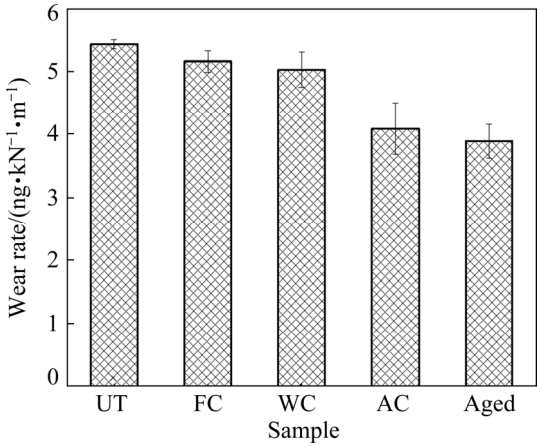

Fig. 11 Wear rate of UT and treated samples under different conditions

wear mechanism whereby trapped debris contributes to the ploughing component of the sample wear. Figures 12(f, g) show a significant amount of trapped debris in the wear tracks of UT and WC samples, respectively.

Similarly, trapped wear debris can be observed in the wear track of the FC sample evident from a large amount of debris, as shown in Fig. 12(i). Furthermore, large grooves can be observed in wear tracks of UT, WC, and FC samples due to the effect of large size of debris, and this contributes to the increased wear rate. Meanwhile, the accumulated or compacted debris observed in the wear track of AC sample exhibited a ductile characteristic, as can be seen from the flow of the buildup debris in Fig. 12(h). This compacted debris contributes little to the three-body abrasive wear, resulting in tribo-film, thereby reducing the wear during sliding. A similar type of debris has also been observed for Ti alloys [50]. However, less debris was observed in the wear track of the aged sample (Figs. 12(e, j)).

Furthermore, the inserts on the left top corner of Figs. 12(f–j) show the backscattered electron (BSE) images revealing the compositional contrast of the wear track to assess any position compositional difference in the wear track. It can be seen that the aged sample shows significant contrast as compared to other samples signifying tribochemical reactions that result in the formation of oxide films. CARQUIGNY et al [51] reported that the Ti−10Zr−10Nb−5Ta exhibited improved tribological properties as compared to the Ti−6Al−4V alloy due to the formation of oxide on the surface; while the low tribological properties of Ti−6Al−4V were attributed to the high reactivity of

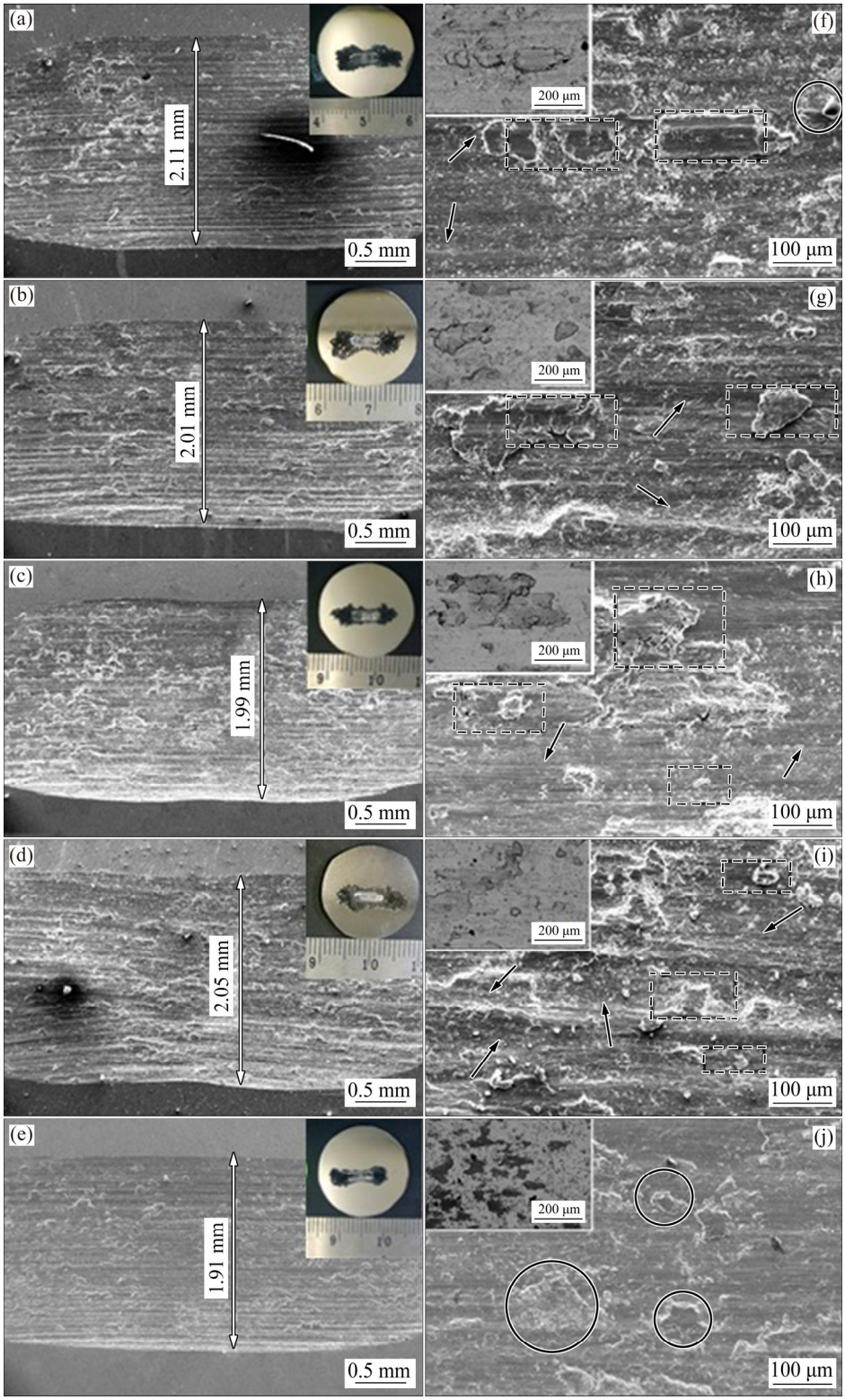

Fig. 12 SEM images of wear tracks of UT (a, f), WC (b, g), AC (c, h), FC (d, i), and aged (e, j) samples (Circles show the oxidized debris, rectangles show the wear debris and arrowheads indicate the grooves)

aluminum resulting in adhesive wear between the sliding parts. EDS analysis of the wear tracks, as shown in Fig. 13, substantiates the presence of oxides, and the oxides are possibly oxides of Ti, Nb, or/and Zr. Fe and Cr observed in the EDS analysis are from the counterface steel ball and may also contribute to the formation of oxides. It should be noted that the UT and WC samples demonstrate

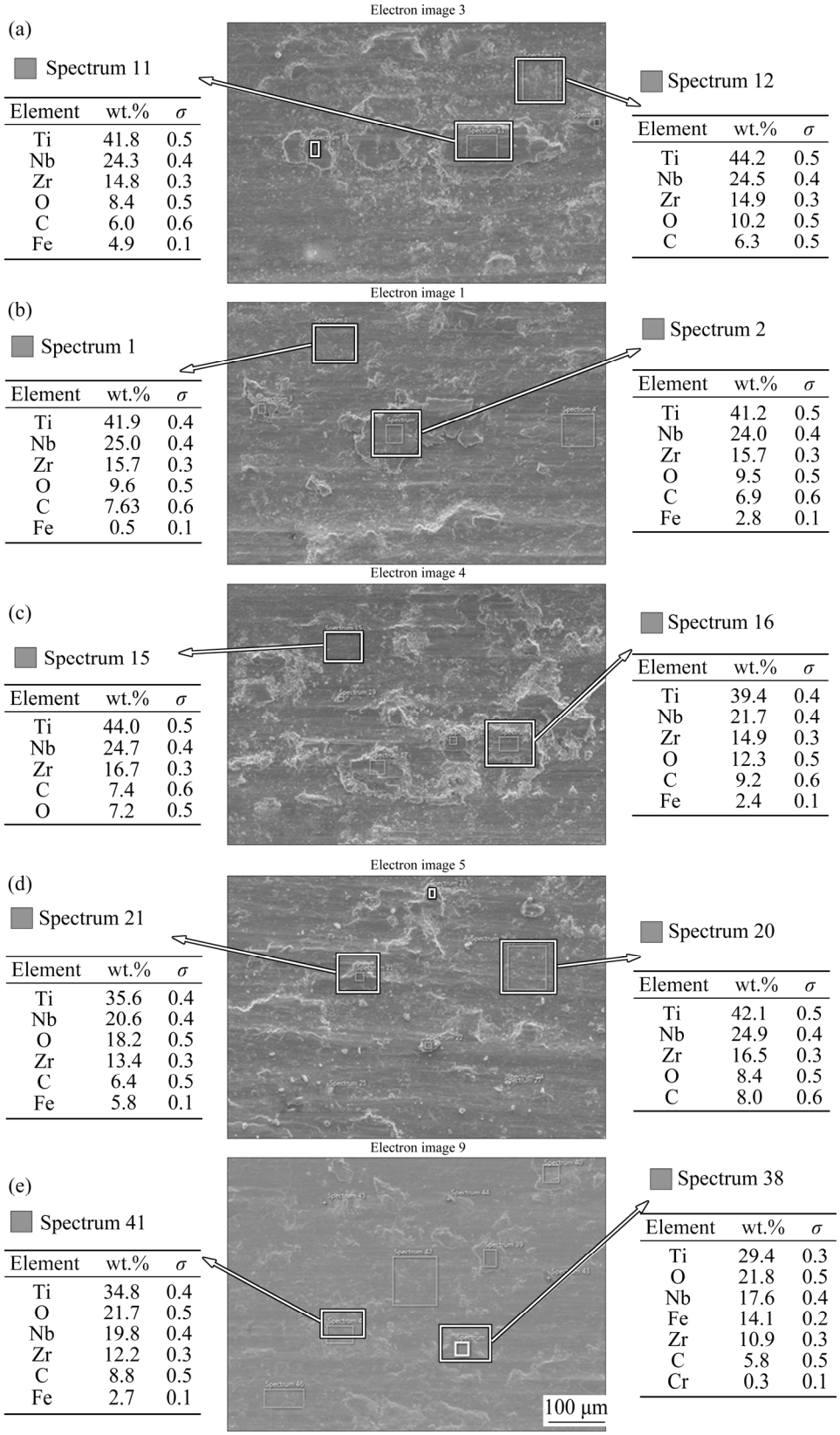

Fig. 13 EDS analysis results of wear tracks of UT (a), WC (b), AC (c), FC (d), and aged (e) samples

mainly abrasive wear with slight oxidation, as evident from the EDS analysis (Figs. 13(a, b)). This is evident from the similar oxygen composition in the wear track and debris, illustrating uniform oxidation but with lower oxygen content. However, a substantial difference in the oxygen composition

exists between the debris and the wear track of samples AC and FC, as in Figs. 13(c, d), respectively. This may illustrate that the oxide films are less adhesive and are easily worn off during sliding. Contrastingly, the wear track and little debris observed for the aged sample (Fig. 13(e)) exhibit similarly high oxygen content. This affirms the uniform oxidation of the wear track and that the oxides are good adherent. This preferential oxidation can also be attributed to the precipitation of the fine α phase in the β matrix during aging. The α phase is known to be more stable and exhibits improved mechanical properties [40]. Thus, based on the BSE images and the EDS analysis, the aged sample shows the highest oxidation, which might be associated with the improved wear resistance. The formation of the adhesive and dense oxide film, coupled with the enhanced mechanical properties, can be instrumental in limiting the abrasive component of the wear and overall improve the wear resistance.

4 Conclusions

(1) The aged and AC TNZ samples exhibited higher microhardness and macrohardness than the WC and FC samples.

(2) The tribological properties of the untreated sample were slightly improved to approximately 5% and 7.5% for the FC and WC samples, respectively. Further improvement in the wear resistance to around 25% and 30% was attained for the AC and aged samples, respectively. However, the coefficient of friction was not influenced by the heat treatment.

(3) The wear mechanism was primarily abrasive wear, while the formation of oxide film on the AC and aged samples coupled with improved mechanical properties can be instrumental in improving the wear resistance.

(4) The aged sample showed the highest microhardness and macrohardness, wear resistance (increased by 30%), and reduced corrosion rate (50%) for long immersion time of up to 168 h in AS.

(5) The improvement in hardness, corrosion, and wear resistance of the thermally treated samples compared to the untreated alloy makes the thermally treated TNZ alloy a viable candidate for dental applications.

Acknowledgments

The authors would like to acknowledge the funding support providing by King Fahd University of Petroleum & Minerals through Project (SR161015).

References

[1] MARECI D, CHELARIU R, BOLAT G, CAILEAN A, GRANCEA V, SUTIMAN D. Electrochemical behaviour of Ti alloys containing Mo and Ta as β-stabilizer elements for dental application [J]. Transactions of Nonferrous Metals Society of China, 2013, 23: 3829−3836.

[2] HUSSEIN M, SURYANARAYANA C, AL-AQEELI N. Fabrication of nano-grained Ti−Nb Zr biomaterials using spark plasma sintering [J]. Materials & Design, 2015, 78: 693−700.

[3] ALI M, HUSSEIN M, AL-AQEELI N. Magnesium-based composites and alloys for medical applications: A review of mechanical and corrosion properties [J]. Journal of Alloys and Compounds, 2019, 792: 1162−1190.

[4] LICAUSI M, IGUAL M A, AMIGÓ BORRÁS V. Influence of the fabrication process and fluoride content on the tribocorrosion behaviour of Ti6Al4V biomedical alloy in artificial saliva [J]. Journal of the Mechanical Behavior of Biomedical Materials, 2013, 20: 137−148.

[5] HASHMI L, WADOOD A. Microstructural, mechanical and shape memory characterizations of Ti−Mo−Sn alloys [J]. Transactions of Nonferrous Metals Society of China, 2020, 30: 688−700.

[6] BHOLA R, CHANDRA C, ALABBAS F M, KUNDU S K, MISHRA B, OLSON D L. Corrosion response of Ti6Al4V and Ti15Mo dental implant alloys in the presence of Listerine oral rinse [J]. International Journal of Corrosion, 2013, 2013: 739841.

[7] YAMAZOE J, MASAHARU A, YOSHINARI M, AKARI T, KUNIO I. The development of Ti alloys for dental implant with high corrosion resistance and mechanical strength [J]. Dental Materials Journal, 2007, 26: 260−267.

[8] MELLADO-VALERO A, MUÑOZ A I, PINA V G, SOLA-RUIZ M F S. Electrochemical behaviour and galvanic effects of titanium implants coupled to metallic suprastructures in artificial saliva [J]. Materials, 2018, 11: 171.

[9] HUANG H H, SHJAU D K, CHEN C S, CHANG J C, WANG S, PAN H, WU F. Nitrogen plasma immersion ion implantation treatment to enhance corrosion resistance, bone cell growth, and antibacterial adhesion of Ti−6Al−4V alloy in dental applications [J]. Surface and Coatings Technology, 2019, 365: 179−188.

[10] BIESIEKIERSKI A, WANG J, GEPREEL M, WEN C. A new look at biomedical Ti-based shape memory alloys [J]. Acta Biomaterialia, 2012, 8: 1661−1669.

[11] CHANDRA R, KARRA P, SHROTRIYA P, VIGGO T, GAISSER M, WEIK T. Life expectancy of modular Ti6Al4V hip implants: Influence of stress and environment [J]. Journal of the Mechanical Behavior of Biomedical Materials, 2011, 8: 1990−2001.

[12] HUSSEIN M, ABDULSAMAD M, AL-AQEELI N. Wear characteristics of metallic biomaterials: A review [J]. Materials, 2015, 8: 2749−2768.

[13] CUI W F, JIN Z, GUO A H, ZHOU L. High temperature deformation behavior of α+β-type biomedical titanium alloy Ti−6Al−7Nb [J]. Materials Science and Engineering A, 2009, 499: 252−256.

[14] HUSSIEN M, AL-AQEELI N. Titanium alloys for biomedical applications and fabrication methods thereof: US patent, 9828655 [P]. 2017.

[15] HUSSEIN M, KUMAR M, DREW R, AL-AQEELI N. Electrochemical corrosion and in vitro bioactivity of nano-grained biomedical Ti−20Nb−13Zr alloy in a simulated body fluid [J]. Materials, 2017, 11: 1−15.

[16] UWAIS Z, HUSSEIN M, ABDULSAMAD M, AL-AQEELI N. Surface modification of metallic biomaterials for better tribological properties: A review [J]. Arabian Journal for Science and Engineering, 2017, 42: 4493−4512.

[17] PRIMA F, DEBUIGNE J, BOLIVEAU M, ANSEL D. Control of omega volume fraction precipitated in a beta titanium alloy: Development of an experimental method [J]. Journal of Materials Science Letters, 2000, 19: 2219−2221.

[18] ZHANG X B, XUE Y J, WANG Z Z. Effect of heat treatment on microstructure, mechanical properties and in vitro degradation behavior of as-extruded Mg−2.7Nd−0.2Zn−0.4Zr alloy [J]. Transactions of Nonferrous Metals Society of China, 2012, 22: 2343−2350.

[19] NAG S, BANERJEE R, FRASER H. Microstructural evolution and strengthening mechanisms in Ti−Nb−Zr−Ta, Ti−Mo−Zr−Fe and Ti−15Mo biocompatible alloys [J]. Materials Science and Engineering C, 2005, 25: 357−362.

[20] CHUNBO L, FENG C, HUIJUAN C, YULONG W, XIANGWEI W. Influence of oxygen content on the microstructure and mechanical properties of cold rolled Ti−32.5Nb−6.8Zr−2.7Sn−xO alloys after aging treatment [J]. Journal of Materials Science & Technology, 2018, 34: 2100−2106.

[21] EL-BAGOURY N, IBRAHIM K. Microstructure, phase transformations and mechanical properties of solution treated bi-modal β titanium alloy [J]. International Journal of Engineering Sciences & Research Technology, 2016, 5: 517−525.

[22] COSTA F H, SALVADOR A F, MELLO M G, GARAM R. Alpha phase precipitation in Ti−30Nb−1Fe alloys—Phase transformations in continuous heating and aging heat treatments [J]. Materials Science and Engineering A, 2016, 677: 222−229.

[23] LI C, CHEN J, LI W, REN Y J, HE J J, SONG Z X. Effect of heat treatment variations on the microstructure evolution and mechanical properties in a β metastable Ti alloy [J]. Journal of Alloys and Compounds, 2016, 684: 466−473.

[24] GALARRAGA H, ROBERT J, WARREN A, LADOS R, MICHAEL M, PEEYUSH N. Effects of heat treatments on microstructure and properties of Ti−6Al−4V ELI alloy fabricated by electron beam melting (EBM) [J]. Materials Science and Engineering A 2017, 685: 417−428.

[25] OKAZAKI Y. A new Ti−15Zr−4Nb−4Ta alloy for medical applications [J]. Current Opinion in Solid State and Materials Science, 2001, 5: 45−53.

[26] MA L W, CHENG H S, CHUNG C Y, YUAN B. Effect of heat treatment time on microstructure and mechanical properties of Ti−19Nb−9Zr (at%) shape memory alloy [J]. Materials Science and Engineering A, 2013, 561: 427−433.

[27] HUSSEIN M, KUMAR M, AL-AQEELI N, ANKAH N, SOROUR A. Influence of thermal treatment on the microstructure, mechanical properties, and corrosion resistance of newly developed Ti20Nb13Zr biomedical alloy in a simulated body environment [J]. Journal of Materials Engineering and Performance, 2019, 28: 1337−1349.

[28] LEE T H, WANG C C, HUANG J K, CHEN L K, CHOU M Y, HUANG H H. Corrosion resistance of titanium-containing dental orthodontic wires in fluoride-containing artificial saliva [J]. Journal of Alloys and Compounds, 2009, 488: 482−489.

[29] ZHANG B B, ZHENG Y F, LIU Y. Effect of Ag on the corrosion behavior of Ti−Ag alloys in artificial saliva solutions [J]. Dental Materials, 2009, 25: 672−677.

[30] LI S J, YANG R, NIINOMI M, HAO Y L, CUI Y Y, GU Z X. Phase transformation during aging and resulting mechanical properties of two Ti−Nb−Ta−Zr alloys [J]. Materials Science and Technology, 2005, 21: 678−686.

[31] GEETHA M, SINGH A, GOGIA A, ASOKAMANI R. Effect of thermomechanical processing on evolution of various phases in Ti−Nb−Zr alloys [J]. Journal of Alloys and Compounds, 2004, 384: 131−144.

[32] MADSEN A, ANDRIEU E, GHONEM H. Microstructural changes during aging of a near-α titanium alloy [J]. Materials Science and Engineering A, 1993, 171: 191−197.

[33] AHMED T, LONG M, SILVERSTRI, RUIZ C, RACK H, BANIA P, EVANS W, FLOWER H. A new low modulus, biocompatible titanium alloy [C]//Titanium 95: Science and Technology. London, UK: IOM, 1995: 1760−1767.

[34] BEEN J, GRAUMAN J. Titanium and titanium alloys, Uhlig's corrosion handbook [M]. New York: John & Wiley, Inc, 2000.

[35] NIINOMI M. Mechanical properties of biomedical titanium alloys [J]. Materials Science and Engineering A, 1998, 243: 231−236.

[36] COLLINGS E. Physical metallurgy of titanium alloys [M]. OH: ASM, Metals Park, 1984.

[37] SONG Y, XU D S, YANG R. Theoretical study of the effects of alloying elements on the strength and modulus of b-type bio-titanium alloys [J]. Materials Science and Engineering A, 1999, 260: 269−274.

[38] TALIB M, KHAN Z, GEETHA M, ARSHAD S. Microstructure, mechanical properties and electrochemical behavior of a novel biomedical titanium alloy subjected to thermo-mechanical processing including aging [J]. Journal of Alloys and Compounds, 2015, 634: 272−280.

[39] NAG S, BANERJEE R, FRASER H. A novel combinatorial approach for understanding microstructural evolution and its relationship to mechanical properties in metallic biomaterials [J]. Acta Biomaterialia, 2007, 73: 369−376.

[40] BANERJEE D, KRISHNAN R. Challenges in alloy design: Titanium for the aerospace industry [C]//Proceedings of the Indian Academy of Sciences Section C: Engineering Sciences. Bengaluru, India: Indian Academy of Sciences, 1981: 21−39.

[41] DONG H C, FENG Z H, LIANG S X, SUN X Y, LI J H, WU D Y, SU R, ZHANG X Y. Evolution of microstructure, mechanical properties and corrosion behaviors using cooling rate regulation in a novel ZrTi-based alloy [J]. Journal of Materials Research and Technology, 2020, 9: 3471−3480.
[42] MANIKA I, MANIKS J. Size effects in micro- and nano-scale indentation [J]. Acta Materialia, 2006, 54: 2049−2056.
[43] GERBERICH W, TYMIAK I, GRUNLAN C, HORSTEMEYER F, BASKES I. Interpretations of indentation size effects [J]. Journal of Applied Mechanics, 2002, 69: 433−442.
[44] LI H, GHOSH A, HAN N, BRADT C. The frictional component of the indent of the indentation size effect in low load microhardness testing [J]. Journal of Materials Research, 1993, 8: 1028−1032.
[45] NI X D, GAO H. Indentation size effects in crystalline materials: A law for strain gradient plasticity [J]. Journal of the Mechanics and Physics of Solids, 1998, 46: 411−425.
[46] HUSSEIN M, SURYANARAYANA C, KUMAR A, AL-AQEELI N. Effect of sintering parameters on microstructure, mechanical properties and electrochemical behavior of Nb−Zr alloy for biomedical applications [J]. Materials & Design, 2015, 83: 344−351.
[47] LU Y J, GUO S, YANG Y, LIU Y J, YU Z, WU Q W, ZHAO C Q, LIN J X. Effect of thermal treatment and fluoride ions on the electrochemical corrosion behavior of selective laser melted CoCrW alloy [J]. Journal of Alloys and Compounds, 2018, 730: 552−562.
[48] BANUMATHY S, PRASAD K S, MANDAL R K, SINGH A K. Effect of thermomechanical processing on evolution of various phases in Ti−Nb alloys [J]. Bulletin of Materials Science, 2011, 34: 1421−1434.
[49] MOHAMMED T, GEETHA M. Effect of thermo-mechanical processing on microstructure and electrochemical behavior of Ti−Nb−Zr−V new metastable β titanium biomedical alloy [J]. Transactions of Nonferrous Metals Society of China, 2015, 25: 759−769.
[50] CHOUBEY A, BIKRAMJIT B, BALASUBRAMANIAM R. Tribological behaviour of Ti-based alloys in simulated body fluid solution at fretting contacts [J]. Materials Science and Engineering A, 2004, 37: 234−239.
[51] CARQUIGNY S, TAKADOUM J, IVANESCU S. Comparative study of nitrogen implantation effect on mechanical and tribological properties of Ti−6Al−4V and Ti−10Zr−10Nb−5Ta alloys [J]. The European Physical Journal Applied Physics, 2019, 85: 21301.

热处理改善齿科用钛合金的体外腐蚀、磨损和力学性能

Mohamed HUSSEIN[1], Akeem Y. ADESINA[1], Madhan KUMAR[1],
Mohamed AZEEM[2], Ahmad SOROUR[1,2], Nasser AL-AQEELI[3]

1. Center of Research Excellence in Corrosion, King Fahd University of Petroleum & Minerals, Dhahran 31261, Saudi Arabia;
2. Department of Mechanical Engineering, King Fahd University of Petroleum & Minerals, Dhahran 31261, Saudi Arabia;
3. Mechanical Engineering Department, College of Engineering, King Saud University, Riyadh 11421, Saudi Arabia

摘　要：研究热处理对新型 Ti20Nb13Zr (TNZ)合金组织、力学性能、耐磨性和人工唾液(AS)体外腐蚀防护性能的影响。采用 X 射线衍射(XRD)、扫描电镜(SEM)等进行结构和显微组织分析。采用电化学阻抗谱和线性极化电阻技术研究样品在 AS 中浸泡 168 h 后的体外耐腐蚀性能。采用线性往复摩擦计对其摩擦特性进行研究。SEM 分析结果表明，固溶处理和时效影响 α 相的尺寸和分布。空冷和时效处理后样品具有最高的显微硬度和宏观硬度，其耐磨性分别比未处理样品高 25%和 30%。冷却速率对 TNZ 合金的耐腐蚀性有显著影响。经过处理的样品在 AS 中浸泡 168 h 后，腐蚀速率降低 50%。经炉冷和时效处理的样品在 AS 中浸泡 168 h 后具有最好的耐腐蚀性。在经过处理的样品中，时效样品表现出更优异的力学性能、耐磨性能和体外耐腐蚀性能。

关键词：热处理；钛基合金；显微组织；力学性能；磨损；腐蚀；生物材料

(Edited by Wei-ping CHEN)